SYNTHETIC APERTURE ANALYSIS OF MULTIPATH PROPAGATION IN THE ULTRA-WIDEBAND COMMUNICATIONS CHANNEL

Wasim Q. Malik, Christopher J. Stevens, and David J. Edwards
Department of Engineering Science, University of Oxford, Parks Road, Oxford OX1 3PJ, U.K.
Email: {wasim.malik, christopher.stevens, david.edwards}@eng.ox.ac.uk

ABSTRACT

We discuss synthetic aperture techniques for radio imaging and direction-of-arrival (DoA) analysis in an indoor ultra-wideband (UWB) environment. A wavefront reconstruction technique is used for visual representation of time-evolutionary wave traversal, and optical diffraction theory is used to transform complex channel data from a rectilinear synthetic aperture into its angular spectrum. Using this analysis with measured channel data, the DoA properties of UWB propagation are investigated. It is demonstrated that the channel experiences strong angular clustering in general. Initial evidence of frequency selective scattering is also reported. The significance of these results for beam-forming, diversity and MIMO systems is highlighted.

1. INTRODUCTION

A dense multipath wireless channel is characterized by a large number of multipath components. The directions-of-arrival (DoA) of these multipaths identify the angular locations of the scatterers in the propagation environment. This provides additional information for the resolution of concurrently received multipaths and helps reduce fading. Array communications and radar systems use it for beam- and null-steering to improve signal-to-noise ratio and overcome jamming and interference. Some of the composite received multipaths in the indoor channel remain unresolved [1]. Since it is improbable for concurrent multipaths to share the azimuth and elevation angles, DoA-based multipath resolution becomes useful. Channel DoA characterization is therefore a topic of keen interest. Uniform, Laplacian and Gaussian distributions have been used to model the indoor channel's angular properties [2].

In this paper, the ultra-wideband (UWB) indoor channel is subjected to DoA analysis. UWB signals have very wide spectra, providing gigabit capacities on short-range indoor radio networks besides increased robustness and interference rejection [3, 4]. The high temporal resolution, in addition to reducing fading, yields high spatial and angular resolution important for imaging applications. We discuss some fundamental techniques for UWB DoA calculation in time and frequency domains. Aided with synthetic aperture measurement data, time- and frequency-domain DoA analysis is performed through wavefront reconstruction and the Fourier transform respectively. The results for line-of-sight and non-line-of-sight scenarios and across frequencies are compared, and their implications for modern multi-antenna communications systems are discussed.

2. EXPERIMENTAL CONFIGURATION

Synthetic aperture measurements were conducted in a typical indoor environment shown in Fig. 1. A vector network analyzer (VNA) logged the complex frequency transfer function $S_{21}(f)$ [5]. The cables were calibrated to compensate for frequency-variant attenuation and phase distortion. The UWB band (f_l = 3.1 to f_h = 10.6 GHz) was sounded with n_f = 1601 discrete frequencies at Δf = 4.7 MHz intervals. A square grid arrangement was used to construct a virtual array, and the receive antenna was placed on a computer-controlled xy-positioner. The dimensions of the array in each direction were $n_x = n_y$ = 100 elements with a uniform spacing of d = 0.01 m. This dense spacing met the spatial Nyquist resolution criterion for f_h, i.e. $d \le \lambda_h/2$. The aperture size was chosen to meet the condition $n_x \ge 10\lambda_l$ so that important features of the wavefront propagation were recorded. Omni-directional discone antennas were used at the both ends to mimic the broadcast configuration commonly used in indoor wireless networks. The vertically polarized antennas were hoisted at a height of 1.5 m above the floor. The distance between the transmit antenna and the centre of the grid was 4.5 m. A large rectangular aluminum sheet connected to the common electrical ground was placed between the antennas for the NLOS measurement. Using this setup, the complex channel transfer function at each grid location was recorded:

$$\tilde{H}(x,y,f) = a_{x,y,f} e^{j\gamma_{x,y,f}}, \qquad (1)$$

where $a_{x,y,f}$ and $\gamma_{x,y,f}$ are the measured magnitude and phase responses at frequency f on grid position (x, y).

3. WAVEFRONT RECONSTRUCTION

Wavefront reconstruction imaging provides a visual representation of time-evolutionary wave propagation, giving information about the sequence and directions of multipath arrivals, their intensities, and the resulting interference patterns across the measurement grid. The complex transfer function in (1) is converted to the channel impulse response

$$\tilde{h}(x,y,\tau) = \alpha_{x,y,\tau}\delta\left(\tau - \tau_{x,y,\tau}\right)e^{j2\pi f\tau_k}, \quad \forall\ 0 \le \tau \le \tau_s \qquad (2)$$

where τ is the time delay and

$$\tau_s = \tau_p + \tau_w \qquad (3)$$

is the symbol time which is the sum of the propagation delay and the delay profile width. Note that here τ = 0 is defined as the time of transmission and not the time of first arrival. The impulse response $\tilde{h}(x,y,\tau)$ corresponding to a point at the centre of the grid is shown in Fig. 2. There are a large number of resolved multipaths, and τ_p is about 70 ns. From the plot, the

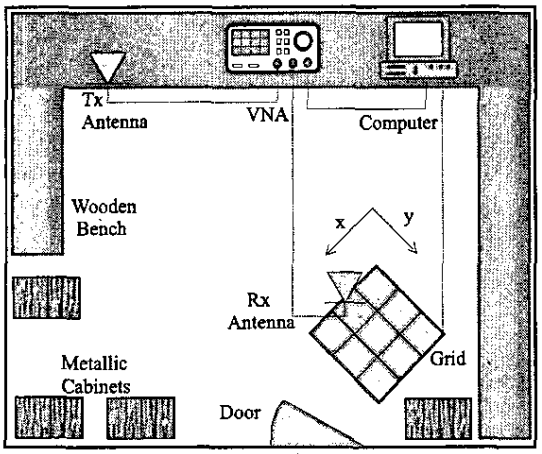

Fig. 1. Synthetic aperture indoor channel measurement system

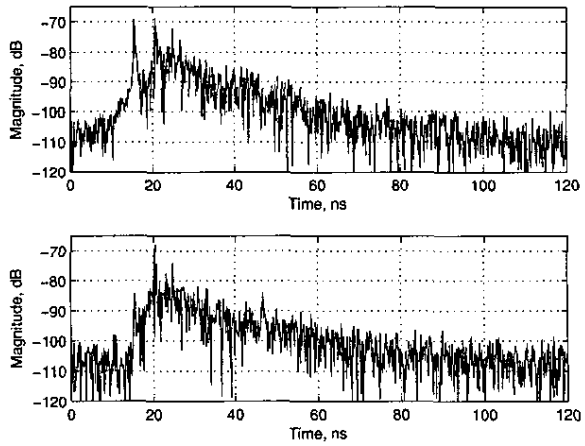

Fig. 2. Measured channel impulse response at centre of grid (a) Line-of-sight; (b) Non-line-of-sight

LOS and NLOS channel responses are similar except that the first path in the latter is highly attenuated, as expected.

The impulse response magnitude gives the waveform intensity as a function of space (x, y) and time τ, i.e.,

$$\left|\tilde{h}(x,y,\tau)\right| = \alpha_{x,y,\tau}\delta\left(\tau - \tau_{x,y,\tau}\right). \tag{4}$$

The values of $\left|\tilde{h}(x,y,\tau)\right|$ corresponding to successive values of τ at all antenna elements in the measurement grid provide a simple implementation of wavefront reconstruction imaging. Sequential images of the CIR at each point are obtained corresponding to various time delay bins. Four time-domain snapshots for LOS and NLOS are captured in Figs. 3 and 4, showing the area of the grid where the x- and y-axes are as defined in Fig. 1. Given the transmitter–receiver antenna separation, the propagation delay of the direct path is expected to be τ_0 =15 ns, therefore this is chosen as the first instant to analyze the time-domain image, and subsequent images are formed at intervals that allow sufficient variation, so that τ_i = {15, 20, 25, 30} ns. Each image is thresholded to -25 dB below the LOS peak power level for noise suppression. High intensity is indicated by brightness in these figures.

In the LOS case, Fig. 3, the first snapshot at τ_0 = 15 ns shows the direct component, which has a strong, well-defined wavefront. It appears curved since the transmitter lies in the near field of the synthetic aperture as discussed in the next section. Close inspection reveals that it is actually a cluster of multiple closely arriving waves, led by the direct, dominant multipath component which is followed by several lower intensity waves. The wavefronts are concentric, indicating that they are produced by co-located scatterers in close proximity to the transmitter. This is also confirmed by the small difference in their times of arrival. In Fig. 4(a), the NLOS system receives only a wave that is 15 dB lower than its LOS counterpart, and is actually the leakage power from the blocked direct path in accordance with the observations of Fig. 2. The second strong wave reaches the receiver at τ_1 = 20 ns in Fig. 3(b), with the same trajectory as the direct component. As it is identical to Fig. 4(b) in shape and intensity, it is unlikely to be a reflection from the transmitter's back wall traveling in the same direction as the direct path, which would also have been blocked by the screen in the NLOS measurement. Therefore it is possibly a reflection from either the floor or the ceiling. Hemispheric elevation discrimination, however, is not directly available without a synthetic volume measurement. Because of the additional path-length, the wavefront appears less circular, approaching the array far-field condition. The next frame at τ_2 = 25 ns shows a case where an interference pattern has been created due to the effect of many waves, out of which two are dominant. The two waves do not overlap at the centre of the grid at τ_2. A comparison with Fig. 2 leads us to believe that the two waves are the two strong paths seen in the impulse response close to 25 ns. One of the waves is traveling away from the transmitter in a slant along the direction of the (0, 100), (100, 0) diagonal, while the other is traveling perpendicular to it approaching the origin. At τ_3 = 30 ns, the residual effect of waves from multiple reflections is seen. An almost random interference pattern is created, and no single dominant wave is present. This, like the two preceding cases, is identical for the LOS and NLOS situations.

4. SINGLE-FREQUENCY ANGULAR SPECTRA

The far-field radiation pattern can be constructed using synthetic aperture back-propagation, which produces an image of the multipath propagation environment in the (θ, φ) plane [6].

For a uniform linear antenna aperture each of whose N elements, with spacing d, radiates a monochromatic signal $\tilde{s}(n)$, the composite signal reaching a point R in space is

$$\tilde{\zeta}(\gamma) = \sum_{n=0}^{N-1} \tilde{s}(n) e^{-jknd\sin\gamma} e^{j2\pi ft}, \tag{5}$$

where $k = 2\pi/\lambda$, and the position vector $\underline{r} = [x\ y\ 0]$ makes an angle $-\pi/2 \le \gamma \le \pi/2$ with the array. Extending this to rectangular arrays and wideband signals,

$$\tilde{\zeta}(\theta,\varphi,f) = \sum_{x=0}^{n_x-1}\sum_{y=0}^{n_y-1} \tilde{s}(x,y,f) e^{-jk(xd\sin\theta\cos\varphi + yd\sin\theta\sin\varphi)} e^{j2\pi ft}$$

(6)

where the normalization

$$\tilde{s}(x,y,f) = \tilde{H}(x,y,f) f \tag{7}$$

compensates for the frequency-dependent attenuation of omni-directional antennas. It can be immediately recognized that (6) is a two-dimensional Fourier transform operation. The fast Fourier transform (FFT) can indeed be used to calculate the angular

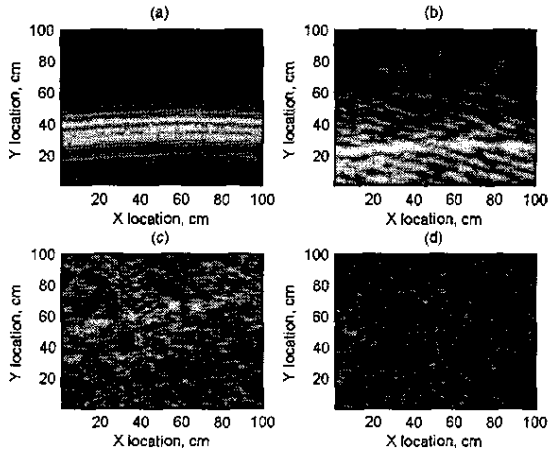

Fig. 3. Wavefront reconstruction imaging for line-of-sight (a) 15 ns; (b) 20 ns; (c) 25 ns; (d) 30 ns

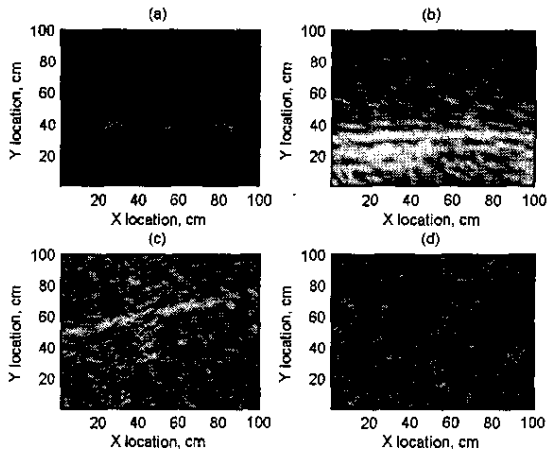

Fig. 4. Wavefront reconstruction imaging for non-line-of-sight (a) 15 ns; (b) 20 ns; (c) 25 ns; (d) 30 ns

spectrum. The 2-D FFT of $\tilde{s}(x,y,f)$ transforms the signal from spatial to wavenumber domain and forms an image of the scatterers in the (k_x, k_y) plane that is actually a polar representation of the (θ, φ) plane angular spectrum:

$$\tilde{\kappa}(k_x,k_y,f)=\frac{1}{n_x n_y}\sum_{x=0}^{n_x-1}\sum_{y=0}^{n_y-1}\tilde{s}(x,y,f)e^{-j2\pi\left(\frac{xk_x}{n_x}+\frac{yk_y}{n_y}\right)}. \quad (8)$$

The k_x and k_y variables provide an indirect measure of the DoAs of incoming wave with respect to the xz- and yz-planes respectively, as they are simply the projections of the wave's k-vector on those planes. With a synthetic volume measurement at n_f frequencies, a set of n_f concentric k-spheres are obtained as the k-domain spectra. The radii of the spheres depend on frequency, and have a non-linear relationship with the elevation angle of arrival as described later by (12). We are, however, restricted here to two dimensions k_x and k_y due to our measurement configuration, and therefore a two-dimensional projection of each of the k-spheres is obtained. The Helmholtz equation

$$\left(\nabla^2+k^2\right)\psi=0 \quad (9)$$

has a spatial solution representing a spherical wave with

$$k^2=k_x^2+k_y^2+k_z^2. \quad (10)$$

For a horizontal plane wave, $\theta = \pi/2$ and thus $k_z = 0$. This is true when the corresponding multipath is located on the

$$k^2=k_x^2+k_y^2 \quad (11)$$

circle. Any multipaths with $\theta \in [0, \pi/2)$ are located inside this circle. Also, the angular locus of the multipath on the circle corresponds to azimuth angle φ.

Fig. 5 and 6 show the wavenumber-domain spectra $\tilde{\kappa}(k_x,k_y,f)$ at f_h. The representation is logarithmic and thresholded to -30 dB below the highest level in order to remove measurement noise. It is noticeable that a majority of the spots are arranged along a circle ($\theta \approx \pi/2$), with some falling inside. The antennas are vertically polarized, and the scatterers (walls, metallic cabinets and other objects) are also vertical, consequently most of the reflected waves remain in the plane of the transmitter and receiver aperture. In Fig. 5, the direct component is the brightest point along the circumference towards the bottom, missing in Fig. 6. Vertically above it is the second strongest multipath, coming from some $\theta<\pi/2$. It corresponds to the second path observed in the figures above, and the k-domain analysis thus confirms that it is a reflection from either the floor or the ceiling. There are several other spots inside the circle corresponding to multipaths arriving at various angles. The loci and energy levels of the reflected paths show remarkable symmetry between LOS and NLOS spectra.

With the condition that $n_x = n_y$, (6) and (8) can be used to formulate the $(k_x, k_y) \rightarrow (\theta, \varphi)$ coordinate transformation

$$\theta=\sin^{-1}\left(\frac{\lambda}{n_x d}\sqrt{k_x^{\,2}+k_y^{\,2}}\right) \quad (12)$$

and

$$\varphi=\tan^{-1}\left(\frac{k_y}{k_x}\right). \quad (13)$$

This procedure provides a more computationally efficient transformation of $\tilde{s}(x,y,f)$ to $\tilde{A}(\theta,\varphi,f)$ through the two-dimensional spatial FFT [7] as compared to the full-wave imaging methods [8]. From (12), the elevation field-of-view of the aperture is determined by f: at lower frequencies, less information is available for higher squint angles. Note that in order to obtain the angular spectrum as a function of uniformly spaced θ and φ, data gridding is required [9]. Cubic interpolation gridding was used for this purpose, and points on or near the convex hull incorrectly estimated by the gridding algorithm were corrected. Now, the Rayleigh resolution for azimuth angle [6] is

$$\Delta_\varphi = 70\frac{\lambda}{D} \quad (14)$$

where Δ_φ is in degrees, λ is the wavelength and D is the aperture size which is equivalent to the dimensions of a side of the square grid when the wave approaches it normal to that face, such as for the LOS path in our configuration. When the incoming wave has slanting incidence, it perceives a wider aperture and greater resolution is obtained. Thus $\Delta\varphi$ also varies with φ: the highest resolution is obtained at $\varphi = n\pi/4$, $n = \{1, 3, 5, 7\}$, and the lowest at $\varphi = n\pi/2$, $n = \{0, 1, 2, 3\}$. For a wave whose Poynting vector is normal to the aperture, higher frequencies provide greater angular resolution, and $\Delta\varphi \approx 2°$ at $f_h = 10.6$ GHz for our 1 m^2 measurement grid. On the other hand, the angular spectrum suffers from low elevation resolution, decreasing with θ, and an up-down ambiguity due to the horizontal plane measurement.

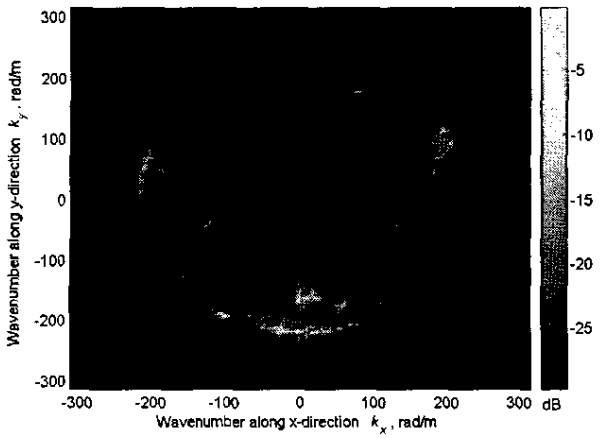

Fig. 5. Wavenumber-domain spectrum for line-of-sight

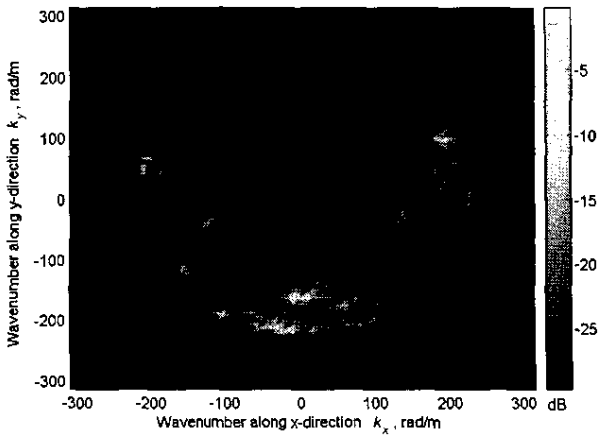

Fig. 6. Wavenumber-domain spectrum for non-line-of-sight

Consequently, $\tilde{A}(\theta,\varphi,f)$ is restricted to $0<\theta\leq\pi/2$, and an elliptical distortion is present in θ, a problem that can be overcome with a synthetic volume aperture. The angular resolution also depends on the far-field condition being satisfied. The Fraunhofer boundary is given by [10]

$$d_f = \frac{2D^2}{\lambda} = \frac{2D^2 f}{c} \tag{15}$$

where c is the speed of light in freespace. For our grid and range of frequencies, d_f varies from 20.67 m to 70.67 m, which is longer than the distance of the receiver antenna from most scatterers. The Fourier transform assumes that all scatterers are located an infinite distance away, which can be approximated with the far field. Since that condition is not strictly met in our scenario, Fresnel diffraction takes place and Fourier transform causes defocusing, resulting in the blurring of incoming beams in the (θ, φ) plane and lesser resolution than predicted by (14). A full-wave treatment carried out using double-convolution [8, 11] rectifies this inaccuracy but is computationally intense.

Fig. 7(a) and (b) show the angular spectra $\tilde{A}(\theta,\varphi,f)$ for LOS and NLOS respectively at the centre frequency (f_c = 6.85 GHz). Both images are normalized with respect to the strongest intensity and are thresholded to -30 dB below that level. The LOS angular spectrum contains the strongest component at (θ, φ) = (90°, -90°), which indeed corresponds to the transmitter location (see Fig. 1) in our synthetic aperture coordinate system. Almost vertically above it are other strong reflections reaching the receiver from about θ = 45°, which corresponds to the reflected signal as seen in the earlier representations. There are multiple, proximal scatterers in the direction of the transmitter, similar to Fig. 3. There are also strong reflections from scatterers located at φ = 30°, 90° and 170°, each in the form of a cluster. There is also some signal arriving from vertically above the receiver, which is smeared horizontally in the image because of the low resolution at low θ. The NLOS angular spectrum is similar to the LOS spectrum, except that the direct component and vertical arrivals are missing. Fig. 8 shows the angular spectra at f_h, normalized to the peak level at this frequency. The contrast has increased, most of the multipaths seen in Fig. 7 now lie below the –30 dB threshold and are suppressed. There is also much higher angular resolution and thus finer spots: clusters from the θ = 90° direction can now be differentiated.

These preliminary results strongly suggest the presence of frequency-selective scattering in the indoor UWB channel. At a physical level, this arises from the non-uniform spatial resolution of the UWB signal's frequency components leading to differential interaction with the propagation environment. Consequently, an object may cause specular reflection at one frequency, scattering at another, and be electromagnetically invisible at yet another. Antennas also cause angular-spectral signal dispersion as shown in [12, 13]. As they are considered a part of the channel in this study, some of the frequency-selectivity observed here can be attributed to them.

5. SYSTEM DESIGN IMPLICATIONS

The findings of this paper are in agreement with the clustered multipath model previously proposed for narrowband indoor channels [2]. Several angularly differentiable multipath clusters are received, and although a probabilistic treatment has not been performed, it appears from inspection that the multipath clusters exhibit non-uniform (possibly Laplacian) angular behavior as reported earlier for narrowband microwave systems [14].

Since in our results there are only about four clusters with strong multipaths, a beam-forming receiver with a suitable beamwidth tuned to only those directions would effectively reject noise and interference, and thus increase SNR or SINR. This can be performed using a beamformer with statistical or eigenvector methods [15, 16].

A clear application of DoA estimation in UWB systems is the ability to reject colored noise and interference. Narrowband interference can be identified from the comparison of the angular spectra corresponding to different frequencies. The power received from an unwanted interference source can then be filtered out in the angular domain with an antenna array, which can complement narrowband interference rejection processing in frequency- or time-domain (such as correlation receivers with pseudorandom noise sequences).

DoA is also important for diversity and multiple-input multiple-output (MIMO) systems [17]. The angular distribution [18] and angular spread [19] of incoming multipaths affect the fading correlation of spatially separated antennas and thus the diversity gain and MIMO capacity. Also, if the clusters are angularly well-separated, an array can be oriented to minimize multipath correlation and increase capacity [20]. From the

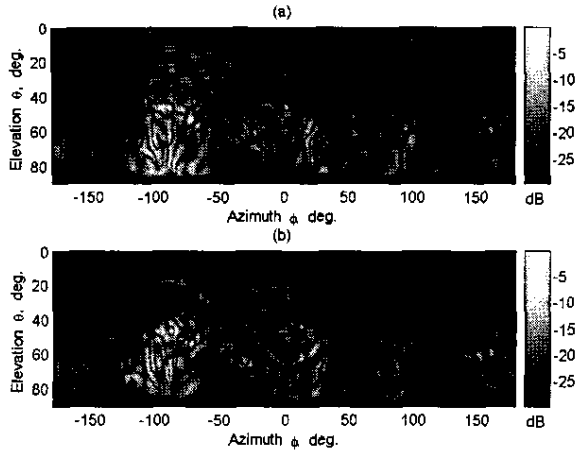

Fig. 7. Peak-normalised angular spectra at centre frequency (6.85 GHz): (a) Line-of-sight; (b) Non-line-of-sight

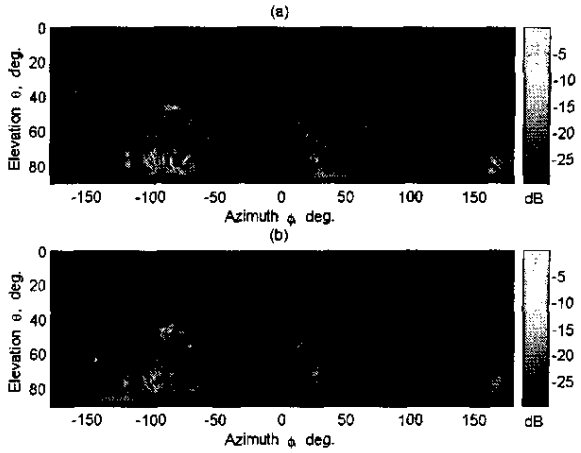

Fig. 8. Peak-normalised angular spectra at highest frequency (10.6 GHz) (a) Line-of-sight; (b) Non-line-of-sight

angular spectra in our results, the multipath clusters can be clearly isolated, indicating that an angular MIMO system can provide a significant capacity gain in a UWB indoor channel. Traditionally MIMO systems are more advantageous in NLOS environments because of higher sub-channel decorrelation. The angular spectra show that NLOS UWB channels experience not only temporal but also angular and spectral decorrelation.

6. CONCLUSION

Multipath directions-of-arrival in the UWB indoor channel have been studied in this paper using line-of-sight and non-line-of-sight synthetic aperture measurements. High temporal and spatial resolution is achieved in UWB time-domain wavefront reconstruction. Frequency-selective and clustered scattering is observed in the angular spectra. Greater contrast and noise rejection is obtained in the upper band. A UWB adaptive beamformer can increase SNR or SINR by rejecting narrowband interference using directional multipath information available for a range of frequencies. Considerable inter-cluster spread leads to low angular multipath fading correlation, high diversity gain and increased MIMO capacity.

7. REFERENCES

[1] H. Hashemi, "The indoor radio propagation channel," *Proc. IEEE*, vol. 81, July 1993.

[2] Q. H. Spencer, B. D. Jeffs, M. A. Jensen, and A. L. Swindlehurst, "Modeling the statistical time and angle of arrival characteristics of an indoor multipath channel," *IEEE J. Select. Areas Commun.*, vol. 18, March 2000.

[3] M. Z. Win and R. A. Scholtz, "Charaterization of ultra-wideband wireless indoor channels: a communication-theoretic view," *IEEE J. Select. Areas Commun.*, vol. 20, December 2002.

[4] S. S. Ghassemzadeh, R. Jana, C. W. Rice, W. Turin, and V. Tarokh, "Measurement and modeling of an ultra-wide bandwidth indoor channel," *IEEE Trans. Commun.*, vol. 52, October 2004.

[5] A. M. Street, L. Lukama, and D. J. Edwards, "On the use of VNAs for wideband propagation measurements," *IEE Proc.-Commun.*, vol. 148, December 2001.

[6] S. Haykin, *Array Signal Processing*. Englewood Cliffs, NJ, USA: Prentice Hall, 1985.

[7] L. Chen and D. J. Edwards, "Applications of non-uniform sampling techniques and fast Fourier transform in plane near field antenna measurements," in *Proc. 8th IEE ICAP*. Edinburgh, UK, March 1993.

[8] H. A. Khan, W. Q. Malik, D. J. Edwards, and C. J. Stevens, "Ultra wideband synthetic aperture image formation techniques," in *Proc. IEE UWBCTSD*. London, UK, 8 July 2004.

[9] W. Q. Malik, H. A. Khan, D. J. Edwards, and C. J. Stevens, "A gridding algorithm for efficient density compensation of arbitrarily sampled Fourier-domain data," in *Proc. IEEE Sarnoff Symp.* Princeton, NJ, USA, April 2005.

[10] J. D. Kraus, *Antennas*, 2nd ed. New York, USA: McGraw-Hill, 1988.

[11] J. G. O. Moss, A. M. Street, and D. J. Edwards, "Wideband radio imaging technique for multipath environments," *Electron. Lett.*, vol. 33, March 1997.

[12] W. Q. Malik, D. J. Edwards, and C. J. Stevens, "Angular-spectral antenna effects in ultra-wideband communications links," *IEE Proc.-Commun.*, (in press).

[13] W. Q. Malik, D. J. Edwards, and C. J. Stevens, "The impact of physical layer frontend characteristics on ultra-wideband radio," in *Proc. 12th Int. Conf. Telecom.* Cape Town, South Africa, May 2005.

[14] C.-C. Chong, C.-M. Tan, D. I. Laurenson, S. McLaughlin, M. A. Beach, and A. R. Nix, "A new statistical wideband spatio-temporal channel model for 5 GHz band WLAN systems," *IEEE J. Select. Areas Commun.*, vol. 21, Feb 2003.

[15] R. A. Monzingo and T. W. Miller, *Introduction to Adaptive Arrays*. New York: John Wiley and Sons, 1980.

[16] A. Haimovich, "Apadtive antenna arrays using eigenvector methods," in *Proc. IEEE ICAP*. Syracruse, NY, USA, June 1988.

[17] W. Q. Malik, M. C. Mtumbuka, D. J. Edwards, and C. J. Stevens, "Performance analysis of ultra-wideband spatial MIMO communications systems," in *Proc. 14th IST Mobile Comm. Summit*. Dresden, Germany, June 2005.

[18] J. Salz and J. H. Winters, "Effect of fading correlation on adaptive arrays in digital mobile radio," *IEEE Trans. Veh. Technol.*, vol. 43, Nov 1994.

[19] L. Chan and S. Loyka, "Impact of multipath angular distribution on performance of MIMO systems," in *Proc. CCECE*. Niagara Falls, Canada, May 2004.

[20] G. Zhao and S. Loyka, "Impact of multipath clustering on the performance of MIMO systems," in *Proc. IEEE WCNC*. Atlanta, GA, USA, March 2004.